Nanoscale

PAPER

View Article Online
View Journal | View Issue

Cite this: *Nanoscale*, 2024, **16**, 10745

Thermal-effect dominated plasmonic catalysis on silver nanoislands†

Ting Kong, [a,b] Bowen Kang,[b] Wei Wang,[c] Tanja Deckert-Gaudig,[c] Zhenglong Zhang *[b] and Volker Deckert *[c,d]

Received 4th January 2024,
Accepted 2nd May 2024

DOI: 10.1039/d4nr00049h

rsc.li/nanoscale

Plasmonic metal nanostructures with the intrinsic property of localized surface plasmon resonance can effectively promote energy conversion in many applications such as photocatalysis, photothermal therapy, seawater desalinization, *etc*. It is known that not only are plasmonically excited hot electrons generated from metal nanostructures under light irradiation, which can effectively trigger chemical reactions, but also plasmonically induced heating simultaneously occurs. Although plasmonic catalysis has been widely explored in recent years, the underlying mechanisms for distinguishing the contribution of hot electrons from thermal effects are not fully understood. Here, a simple and efficient self-assembly system using silver nanoislands as plasmonic substrates is designed to investigate the photo-induced azo coupling reaction of nitro- and amino-groups at various temperatures. In the experiments, surface-enhanced Raman spectroscopy is employed to monitor the time and temperature dependence of plasmon-induced catalytic reactions. It was found that a combination of hot electrons and thermal effects contribute to the reactivity. The thermal effects play the dominant role in the plasmon-induced azo coupling reaction of nitro-groups, which suggests that the localized temperature must be considered in the development of photonic applications based on plasmonic nanomaterials.

Introduction

The unique property of localized surface plasmon resonance (LSPR) on noble metal nanostructures can be used to promote photochemical transformations of micro- or nanomaterials.[1–4] An LSPR is formed by the optical excitation of the collective oscillation of free electrons on the surface of metal nanostructures, which depends on their composition, size, shape, and surrounding medium.[5–9] Simultaneously to the LSPR excitation hot carriers are generated by re-emitting photons or nonradiative Landau damping relaxation.[10–13] In addition, photothermal effects can also be observed. It has been reported that plasmonic hot electrons and thermal effects can trigger photochemical reactions on the surface of the irradiated plasmonic nanostructures.[8,14] Such plasmon-induced photocatalytic reactions have received increasing attention in recent years and are widely applied in water splitting,[15,16] hydrogen production and dissociation,[17,18] photovoltaics,[19] and hydrocarbon conversion.[20,21]

In this contribution, 4-nitrothiophenol (4-NTP) and 4-aminothiophenol (4-ATP) are used as model molecules to study plasmonic photocatalysis under various experimental conditions.[22–25] In the studied molecular catalytic reaction, a photothermal effect is inevitable even under low-power illumination. Consequently, it is challenging to separate this thermal contribution from that of the hot electrons. There are many ongoing investigations focusing on the role of thermal effects by changing the local temperature, for example Kim *et al.* studied the behaviour of 4-NTP and 4-ATP on silver at liquid nitrogen temperature using surface-enhanced Raman scattering (SERS);[26] Golubev *et al.* evaluated the role of plasmonic heating by performing temperature-dependent studies and multi-wavelength analyses.[27] Recently, the evaluation of the temperature directly at a single plasmonic hot-spot was conducted using a Stokes/anti-Stokes Raman approach by considering the Boltzmann distribution and the plasmon resonance profile.[4,28,29] However, the influence of the thermal effects of plasmonic nanostructures during light irradiation has not yet been systematically studied for plasmon-induced catalytic reactions. It is important to note that the size of chemically synthesized plasmonic nanostructures is non-uniform and uncontrollable, which severely limits their application in plasmonic photocatalysis. Therefore, it is an urgent requirement to

[a]*School of Science, Xi'an University of Posts & Telecommunications, 710121 Xi'an, China. E-mail: kongting0302@xupt.edu.cn*
[b]*School of Physics and Information Technology, Shaanxi Normal University, 710119 Xi'an, China. E-mail: zlzhang@snnu.edu.cn*
[c]*Leibniz Institute of Photonic Technology, Albert-Einstein-Str. 9, 07745 Jena, Germany. E-mail: volker.deckert@leibniz-ipht.de*
[d]*Institute of Physical Chemistry and Abbe Center of Photonics, Friedrich Schiller University Jena, Helmholtzweg 4, 07743 Jena, Germany*
† Electronic supplementary information (ESI) available. See DOI: https://doi.org/10.1039/d4nr00049h

systematically explore the effect of the local temperature on the plasmon-induced catalytic reactions by designing a simple and effective photocatalytic system.

In this work, plasmonically active silver nanoislands (AgNIs) were prepared to investigate the role of hot electrons and thermal effects on the photo-induced azo coupling reaction of nitro- and amino-groups at various temperatures using *in situ* SERS monitoring. It is known that 4-NTP and 4-ATP dimerize to dimercaptoazobenzene (DMAB) when adsorbed on plasmonic AgNIs. It was found that the catalytic efficiency of the AgNIs gradually increased with an increase in the surrounding temperature. At 77 K, starting with 4-NTP, DMAB could hardly be detected, but when using 4-ATP, the dimerized product was evident. The results demonstrate that thermal effects dominate in the azo coupling reaction of nitro-groups and hot electrons prevail in the azo coupling reaction of amino-groups. Clearly, the plasmon-induced photocatalytic reaction does not only depend on the hot electrons generated by the metal nanostructure, but also on thermal effects. The results are relevant for the photothermal application of plasmonic nanomaterials and promote the understanding of plasmon assisted catalytic reactions.

Experimental section

Sample preparation

All chemicals were obtained commercially and used without further purification. 80% 4-NTP and 80% 4-ATP were purchased from Sigma-Aldrich. Ethanol was supplied by Sinopharm Chemical Reagent Co., Ltd (China). The glass slides were immersed in a mixed H_2SO_4 (12 mL)/H_2O_2 (28 mL) solution at 80 °C for 2 h, and then washed with ethanol and deionized water. The SERS substrates were prepared by evaporating silver onto precleaned glass slides under high vacuum (2.1×10^{-5} Pa) using a thermal evaporation instrument. The evaporation conditions were carefully controlled to produce a layer of silver film with an average thickness of 5 nm. Then the AgNIs were formed by annealing at 350 °C for 30 s under an argon atmosphere. Finally, the AgNIs were immersed in a 1×10^{-3} M solution of 4-NTP and 4-ATP in ethanol for more than 5 h, then the sample was washed with ethanol for 1 min and dried with N_2 gas.

Material characterization

Atomic force microscopy (AFM) topography images were obtained with a Bruker-JPK NanoWizard Ultras. Extinction spectra were acquired with a PerkinElmer Lambda 950 spectrometer. SERS experiments were performed with a LabRam HR Evolution Raman system (Horiba) with a 50 × (NA = 0.5) objective. The temperature-dependent SERS spectra were measured by using a temperature-controlled Raman cell. 532 nm and 633 nm continuous lasers were employed as excitation sources for the plasmon-induced catalytic reactions. The data acquisition time used in the experiments was 60 s for one spectrum. In order to monitor the reaction dynamic process, very low laser power (1.05 μW–1 mW) was used to obtain the Raman spectra.

Simulations

Numerical simulations were performed by the finite element method with COMSOL Multiphysics. The models of AgNIs formed from Ag NPs with different sizes were constructed according to the experimental geometry. The dielectric constants of the plasmonic silver metal were obtained from the data reported by Johnson and Christy.[30]

Results and discussion

The schematic diagram of the *in situ* plasmonic catalysis reaction of 4-NTP adsorbed on AgNIs is shown in Fig. 1. The AgNIs absorb light and generate hot electrons on the metal surface under LSPR excitation. Then, the hot electrons from the plasmon decay are transferred to the lowest unoccupied molecular orbital of the adsorbed molecule. The $-NO_2$ group is reduced to an –NHOH group in a series of electron and proton transfer steps, which are eventually terminated by a nitrogen–nitrogen coupling.[31] Simultaneously, the photothermal effect of the LSPR relaxation process also favors the conversion of molecules.

The AgNIs substrate preparation method can be found in the Experimental section. As shown in the atomic force microscopy (AFM) topography image in Fig. 2a, the average size of the NPs is about 15 nm (Fig. S1†). The LSPR peak is at 520 nm, which matches well with the irradiation wavelength of 532 nm (Fig. 2b). Under laser excitation, the local temperature generated at a plasmonic NP will increase and is given by eqn (1):[8,32]

$$\Delta T = \frac{\sigma_{abs} I}{4\pi\kappa R} \quad (1)$$

where σ_{abs} is the absorption cross-section of the nanoparticle, I is the irradiance (optical power per unit area), κ is the

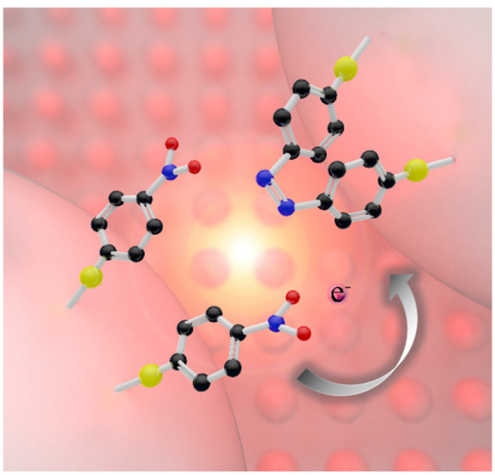

Fig. 1 Scheme of a plasmon-induced catalytic dimerization of 4-NTP to DMAB adsorbed on plasmonic AgNIs. The black, red, blue and yellow spheres represent C, O, N and S atoms, respectively.

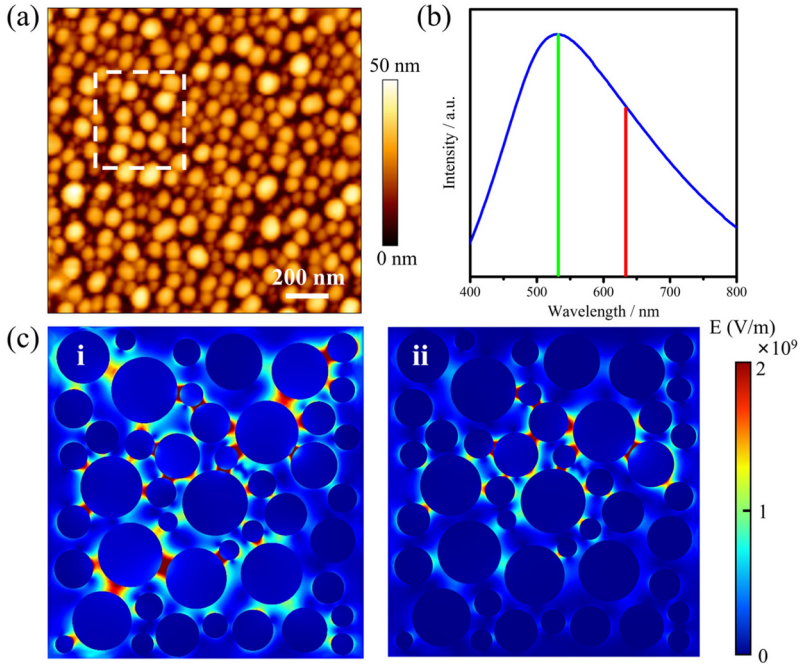

Fig. 2 (a) AFM topography image and (b) normalized extinction spectrum of AgNIs; (c) simulated electric field distribution of AgNIs (a 300 × 300 nm^2 region extracted from the AFM image) under 532 nm (i) and 633 nm (ii) excitation, respectively.

thermal conductivity of the surrounding medium, and R is the radius of the NP. The temperature increase is observed to be directly proportional to the absorption cross-section. According to Fig. 2b, the photothermal effect of AgNIs at 532 nm excitation is better than that at 633 nm excitation. As already mentioned, additional to the plasmonic photothermal effect, hot electrons also contribute to the plasmon-induced catalytic reaction. The total rate of hot electrons generated at a plasmonic NP can be calculated by eqn (2):[33]

$$\mathrm{Rate}_{\text{high-energy}} = \frac{2}{\pi^2} \times \frac{e^2 E_F{}^2}{\hbar} \frac{(\hbar\omega - \Delta E_b)}{(\hbar\omega)^4} \times \int |E_{\text{normal}}(\theta, \varphi)|^2 \mathrm{d}s \quad (2)$$

where ΔE_b is the potential barrier height, E_{normal} is the component of the electric field normal to the surface, and the integral is taken over the entire metal surface. The total rate of hot electrons can be determined by the integration of the $|E_{\text{normal}}|^2$. The simulated electric field distributions of AgNIs under 532 nm and 633 nm excitation are shown in Fig. 2c, respectively, which suggest that the hot electron effect is better at 532 nm excitation than at 633 nm. The results indicate that there is a better photothermal effect and hot electron effect for AgNIs excited at 532 nm than at 633 nm. Such a AgNIs film with high catalytic efficiency was used as the substrate for the following SERS experiments.

Because the LSPR peak of AgNIs is located at around 532 nm, the energy of hot electrons provided by 633 nm excitation is less than that provided by 532 nm. To minimize the contribution of hot electrons, a low laser power at 633 nm was used to study the reaction dynamics in the presence of AgNIs. The time-dependent SERS spectra with 633 nm laser irradiation (7.8 μW) at room temperature (RT) are shown in Fig. 3, where the observation time increases from bottom to top with an interval of 1 min. The graph shows that two 4-NTP molecules dimerized to DMAB gradually during 9 min of irradiation. Prior to the formation of DMAB, the major SERS bands of 4-NTP at 1085, 1336, and 1571 cm^{-1} were assigned to the benzene ring breathing, the $-NO_2$ stretching, and the C–C

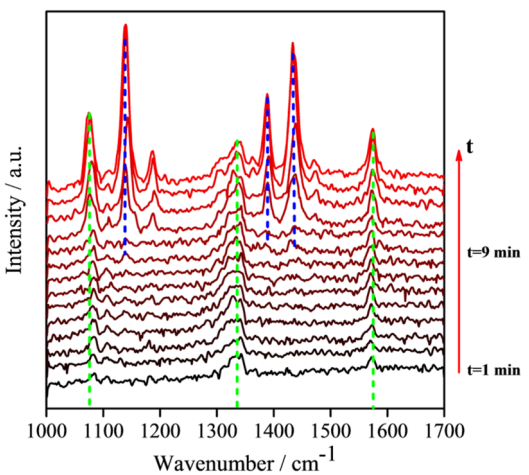

Fig. 3 Time-dependent SERS spectra at room temperature of the reaction of 4-NTP to DMAB on a substrate similar to the one shown in Fig. 2a, at 633 nm excitation. Interval between subsequent spectra is 60 s. (P = 7.8 μW, t_{acq} = 60 s).

stretching mode, respectively. As the photocatalytic reaction proceeded, several new bands at 1140, 1390, and 1438 cm^{-1} were detected, corresponding to the C–N asymmetric stretching, the –N=N– vibration, and the C–H plane bending mode of DMAB, respectively. The dimerization of 4-NTP to DMAB also resulted in significantly stronger SERS signals due to the larger Raman scattering cross-section of DMAB compared to 4-NTP. Moreover, the permanent detection of the band characteristic of 4-NTP at 1336 cm^{-1} indicates an incomplete reaction at room temperature even after 15 min of laser irradiation. Due to the inhomogeneous distribution of AgNIs with different gaps and sizes, the less efficient reaction sites lead to low hot-spot efficiency, thus reducing the catalytic reaction rate.[21]

In order to gain insight into the role of thermal effects on the plasmon-induced catalytic reaction, the system was monitored at cryogenic temperatures as a function of laser power at two excitation wavelengths, 532 nm and 633 nm, respectively. The Raman modes at 1140, 1390, and 1438 cm^{-1} were used to identify the presence of DMAB molecules. As shown in Fig. 4a, it is clear that the plasmon-induced photocatalytic reaction from 4-NTP to DMAB was successful under 532 nm irradiation at −180 °C. Using 633 nm excitation no azo coupling reaction was evident under the same conditions (Fig. 4b). The intensity ratio of 1390 cm^{-1}/1336 cm^{-1} ([DMAB]/[4-NTP]) was then used to determine the catalytic efficiency of plasmonic AgNIs at specific temperatures as shown in Fig. 4c. Clearly, the catalytic efficiency of the AgNIs decreases with the decrease of temperature. At around −150 °C, no DMAB could be synthesized using 633 nm even if the laser power was increased (Fig. S2†). Although 633 nm can excite the plasmons, no azo coupling reaction was observed, because the excitation wavelength was too far from the plasmon resonance maximum. Apparently, a certain thermal effect is necessary. In addition, the energy of the hot electrons produced by the relaxation of the plasmons excited at 633 nm was lower than that with excitation at 532 nm, further resulting in a too low energy to assist the catalytic reaction. Consequently, it is suggested that the thermal effect plays a dominant role in the plasmon-induced coupling reaction of 4-NTP to DMAB.

Besides, temperature-dependent SERS spectra recorded at high temperatures under 532 nm and 633 nm excitation were used to confirm the important role of thermal effects in plasmonic catalysis (see Fig. 5). To ensure that the kinetic process of the catalytic reaction can be monitored at various temperatures, appropriate powers were selected for the 532 nm (1.05 μW) and 633 nm (7.8 μW) excitation light. Similar to the previous experiments, the three characteristic Raman bands at 1140, 1390, and 1438 cm^{-1} were used to monitor the dynamics of the catalytic process. The results show that the 4-NTP dimerized gradually to DMAB with the increase of temperature at 532 nm and 633 nm. The 4-NTP was completely converted to DMAB after irradiating the sample at 100 °C with 532 nm and 633 nm excitation (see Fig. 5a and b). The intensity ratio of 1390 cm^{-1}/1336 cm^{-1} as a function of temperature with 532 nm and 633 nm excitation is shown in Fig. 5c. The slopes of the curves indicate that the catalytic efficiency of AgNIs increased gradually with increasing temperature. It is important to note that no Raman signal was detected at 125 °C using 532 nm excitation. Most likely, the molecules decomposed or detached from the substrate at that high temperature. Since the plasmonic photothermal effect was lower at 633 nm excitation than at 532 nm, the azo coupling reaction was observed with 633 nm irradiation at 100–150 °C. These results suggest that thermal effects can play a dominating role in studying the azo coupling reaction catalyzed by plasmonic AgNIs.

In subsequent experiments, the catalytic reaction of 4-ATP on AgNIs was investigated to further determine the role of thermal effects and hot electrons. The temperature-dependent SERS spectra are shown in Fig. 6. The distinct Raman bands at 1390 and 1438 cm^{-1} corresponding to the N=N stretching and C–H bending vibrations of DMAB were detected over the entire temperature range from −180–250 °C. This observation demonstrates a successful reaction of 4-ATP to DMAB even at 1.05 μW. A similar experimental phenomenon can be observed for the catalytic reaction of 4-ATP on AgNIs excited at 633 nm

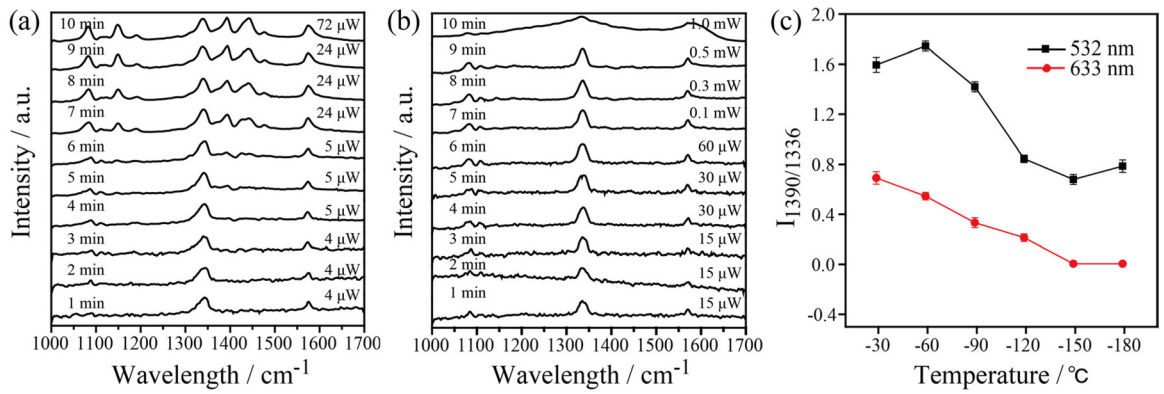

Fig. 4 Time-dependent SERS spectra of the plasmon-induced catalytic reaction of 4-NTP at −180 °C with (a) 532 nm and (b) 633 nm excitation at different laser powers on the samples. The time interval is 1 min from bottom to top, t_{acq} = 60 s; (c) the average intensity ratio of 1390 cm^{-1}/1336 cm^{-1} referring to [DMAB]/[4-NTP] as a function of temperature at 532 nm (black) and 633 nm (red).

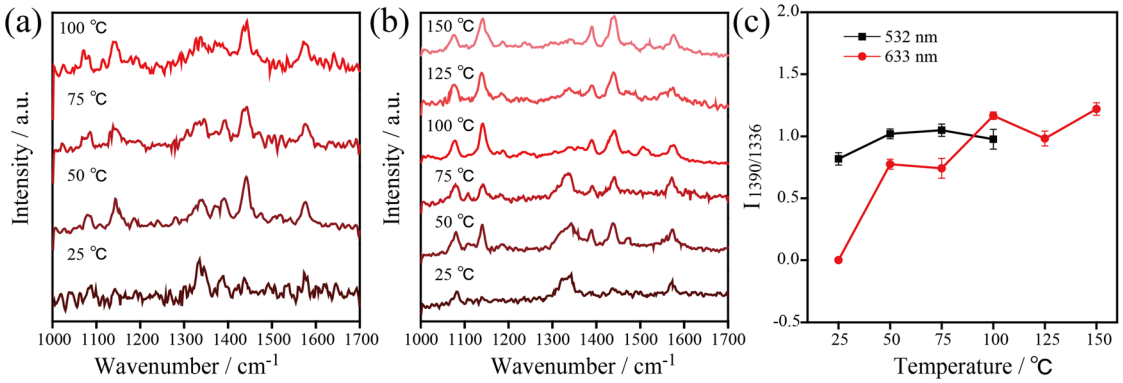

Fig. 5 Temperature-dependent SERS spectra of the plasmon-induced photocatalytic reaction of 4-NTP at high temperatures with 532 nm (a) and 633 nm (b) excitation, respectively, t_{acq} = 60 s. (c) intensity ratio of 1390 cm^{-1}/1336 cm^{-1} referring to [DMAB]/[4-NTP] as a function of temperature at 532 nm (black) and 633 nm (red) ($P_{532\ nm}$ = 1.05 μW, $P_{633\ nm}$ = 7.8 μW).

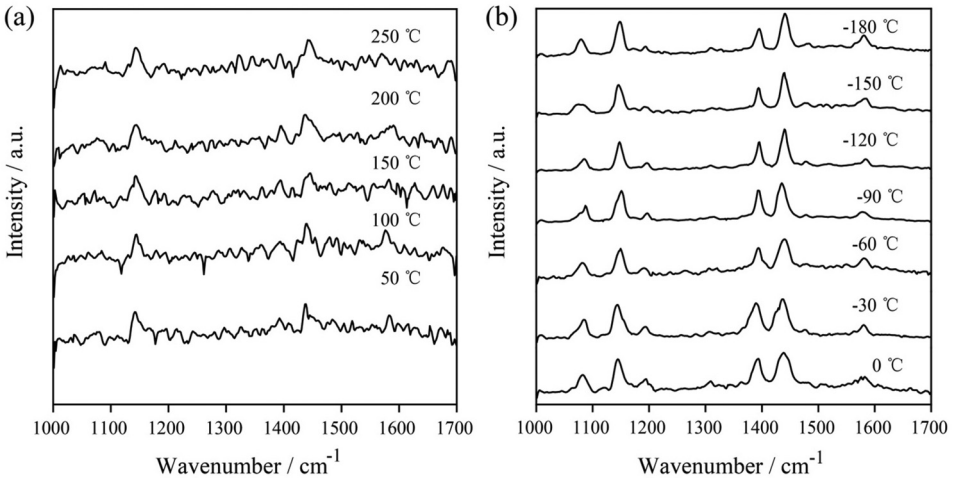

Fig. 6 Temperature-dependent SERS spectra of the plasmon-induced photocatalytic reaction of 4-ATP at 50–250 °C (a) and at −180–0 °C (b) with 532 nm excitation (P = 1.05 μW), t_{acq} = 60 s.

(Fig. S3 and S4†). In contrast to 4-NTP, hot electrons must obviously dominate in the plasmon-induced catalytic reaction of 4-ATP. Due to the lower reaction energy barrier of the azo coupling reaction of amino-groups compared to nitro-groups, 4-ATP molecules can be easily converted to DMAB molecules even at cryogenic temperatures.[23] It is postulated that 4-ATP molecules are not affected by the surrounding temperature, since hot electrons play a more important role in this process.

Conclusions

The plasmonic induced azo coupling reactions of 4-NTP and 4-ATP to DMAB were investigated at 532 nm and 633 nm with surface-enhanced Raman spectroscopy at various temperatures. Using plasmonically active nanoislands on glass substrates enabled the discrimination of hot electron and thermal effects in the catalytic reactions. After evaluating the time-dependent SERS spectra at different temperatures, it was found that the intensity of the Raman bands of DMAB gradually increased at elevated temperatures, indicating the improved catalytic efficiency of AgNIs under these conditions. Interestingly, at −180 °C, 4-NTP hardly reacted to DMAB while 4-ATP completely dimerized to DMAB at such low temperatures. The SERS results demonstrate that the thermal effect is a key parameter in the catalytic reaction of 4-NTP to DMAB while hot electrons dominate in the catalytic dimerization of 4-ATP. Our systematic results based on a temperature-dependent approach at different wavelengths indicate that the photothermal effect plays a significant role in photocatalytic reactions that must be taken into account. This work deepens the understanding of the photocatalytic reaction mechanism and will promote the development of further photonic applications of plasmonic catalysis.

Conflicts of interest

The authors declare no conflict of interest.

Acknowledgements

This work was supported by the National Key R&D Program of China (No. 2020YFA0211300 and 2021YFA1201500), the National Natural Science Foundation of China (No. U22A6005, 92150110 and 12204376), the Fundamental Science Foundation of Shaanxi (No. 22JSZ010), and the Fundamental Research Funds for Central Universities (GK202201012 and GK202308001). We furthermore acknowledge support from the German Science Foundation *via* the Collaborative Research Centers TR 234 CataLight-C1 (WW), SFB 1375 NOA and the individual DFG project No 448666227 (TDG).

References

1 Z. Zhang, C. Zhang, H. Zheng and H. Xu, *Acc. Chem. Res.*, 2019, **52**, 2506–2515.
2 A. Gelle, T. Jin, L. de la Garza, G. D. Price, L. V. Besteiro and A. Moores, *Chem. Rev.*, 2020, **120**, 986–1041.
3 T. Kong, C. Zhang, X. Gan, F. Xiao, J. Li, Z. Fu, Z. Zhang and H. Zheng, *J. Mater. Chem. C*, 2020, **8**, 4338–4342.
4 Z. Zhang, T. Deckert-Gaudig and V. Deckert, *Analyst*, 2015, **140**, 4325–4335.
5 Y. Zhang, S. He, W. Guo, Y. Hu, J. Huang, J. R. Mulcahy and W. D. Wei, *Chem. Rev.*, 2018, **118**, 2927–2954.
6 K. Watanabe, D. Menzel, N. Nilius and H. J. Freund, *Chem. Rev.*, 2006, **106**, 4301–4320.
7 V. A. Spata and E. A. Carter, *ACS Nano*, 2018, **12**, 3512.
8 T. Kong, C. Zhang, J. Lu, B. Kang, Z. Fu, J. Li, L. Yan, Z. Zhang, H. Zheng and H. Xu, *Nanoscale*, 2021, **13**, 4585–4591.
9 J. Dong, W. Zhou, C. Yang, H. Wu, Q. Han, C. Zhang, W. Gao, X. Yan and M. Sun, *ACS Appl. Mater. Interfaces*, 2023, **15**, 28840–28848.
10 M. L. Brongersma, N. J. Halas and P. Nordlander, *Nat. Nanotechnol.*, 2015, **10**, 25–34.
11 V. Amendola, R. Pilot, M. Frasconi, O. M. Marago and M. A. Iati, *J. Phys.: Condens.Matter*, 2017, **29**, 203002.
12 C. Clavero, *Nat. Photonics*, 2014, **8**, 95–103.
13 S. Hashimoto, D. Werner and T. Uwada, *J. Photochem. Photobiol., C*, 2012, **13**, 28–54.
14 C. Zhang, T. Kong, Z. Fu, Z. Zhang and H. Zheng, *Nanoscale*, 2020, **12**, 8768–8774.
15 C. G. Silva, R. Juarez, T. Marino, R. Molinari and H. Garcia, *J. Am. Chem. Soc.*, 2011, **133**, 595–602.
16 D. B. Ingram and S. Linic, *J. Am. Chem. Soc.*, 2011, **133**, 5202–5205.
17 W. S. Zhi, S. Liu, M. Low, S. Y. Zhang, Z. Liu, A. Mlayah and M. Y. Han, *Adv. Mater.*, 2012, **24**, 2310–2314.
18 S. Mukherjee, F. Libisch, N. Large, O. Neumann and N. J. Halas, *Nano Lett.*, 2012, **13**, 240–247.
19 Y. K. Lee, C. H. Jung, J. Park, H. Seo, G. A. Somorjai and J. Y. Park, *Nano Lett.*, 2011, **11**, 4251–4255.
20 W. Hou, W. H. Hung, P. Pavaskar, A. Goeppert, M. Aykol and S. B. Cronin, *ACS Catal.*, 2011, **1**, 929–936.
21 P. Singh, T. Deckert-Gaudig, Z. Zhang and V. Deckert, *Analyst*, 2020, **145**, 2106–2110.
22 B. Dong, Y. Fang, X. Chen, H. Xu and M. Sun, *Langmuir*, 2011, **27**, 10677–10682.
23 L. B. Zhao, M. Zhang, Y. F. Huang, C. T. Williams, D. Y. Wu, B. Ren and Z. Q. Tian, *J. Phys. Chem. Lett.*, 2014, **5**, 1259–1266.
24 Z. Zhang and J. Kneipp, *Anal. Chem.*, 2018, **90**, 9199–9205.
25 S. Van, T. Deckert-Gaudig, A. Mank, V. Deckert and B. M. Weckhuysen, *Nat. Nanotechnol.*, 2012, **7**, 583–586.
26 K. Kim, J.-Y. Choi and K. S. Shin, *J. Phys. Chem. C*, 2014, **118**, 11397–11403.
27 A. A. Golubev, B. N. Khlebtsov, R. D. Rodriguez, Y. Chen and D. R. T. Zahn, *J. Phys. Chem. C*, 2018, **122**, 5657–5663.
28 M. Richard-Lacroix and V. Deckert, *Light: Sci. Appl.*, 2020, **9**, 35.
29 D. P. dos Santos, M. L. Temperini and A. G. Brolo, *J. Am. Chem. Soc.*, 2012, **134**, 13492–13500.
30 P. B. Johnson and R. W. Christy, *Phys. Rev. B: Solid State*, 1972, **6**, 4370–4379.
31 L. B. Zhao, Y. F. Huang, X. M. Liu, J. R. Anema, D. Y. Wu, B. Ren and Z. Q. Tian, *Phys. Chem. Chem. Phys.*, 2012, **14**, 12919–12929.
32 R. Kamarudheen, G. Kumari and A. Baldi, *Nat. Commun.*, 2020, **11**, 3957.
33 X. T. Kong, Z. Wang and A. O. Govorov, *Adv. Opt. Mater.*, 2017, **5**, 1600594.

